# Finite element analysis of CFRP laminate repairs on damaged end regions of prestressed concrete bridge girders

Ian D. Shaw[a] and Bassem Andrawes[*]

*Department of Civil and Environmental Engineering, University of Illinois at Urbana-Champaign, 205 N. Mathews, Urbana, IL 61801, USA*

**Abstract.** Over the past couple decades, externally bonded fiber reinforced polymer (FRP) composites have emerged as a repair and strengthening material for many concrete infrastructure applications. This paper presents an analytical investigation of the use of carbon FRP (CFRP) for a specific problem that occurs in concrete bridge girders wherein the girder ends are damaged by excessive exposure to deicing salts and numerous freezing/thawing cycles. A 3D finite element (FE) model of a full scale prestressed concrete (PC) I-girder is used to investigate the effect of damage to the cover concrete and stirrups in the end region of the girder. Parametric studies are performed using externally bonded CFRP shear laminates to determine the most effective repair schemes for the damaged end region under a short shear span-to-depth ratio. Experimental results on shear pull off tests of CFRP laminates that have undergone accelerated aging are used to calibrate a bond stress-slip model for the interface between the FRP and concrete substrate and approximate the reduced bond stress-slip properties associated with exposure to the environment that causes this type of end region damage. The results of these analyses indicate that this particular application of this material can be effective in recovering the original strength of PC bridge girders with damaged end regions, even after environmental aging.

## 1. Introduction

Much of the existing concrete infrastructure in the United States is near the end of its design life and in need of replacing, rehabilitation, or repair. Over 58,000 bridges have been deemed structurally deficient in 2016 (ARTBA 2016). Many of these structurally deficient bridges are located in the Northeast and Midwest, where harsh climates cause deterioration in concrete structures at an accelerated rate. One specific problem that plagues bridges is the deterioration of the beam's end regions due to failure of expansion joints, which allows water containing deicing salts to flow onto the beam ends. Freezing and thawing cycles of these saturated beam ends cause scaling and spalling of the cover concrete. This can directly expose the steel reinforcement to chlorides, which can lead to severe corrosion and further spalling of concrete. Because of the

---

∗Corresponding author, Associate Professor, E-mail: andrawes@illinois.edu
[a]M.S. Student, E-mail: ianshaw2@illinois.edu

localized nature of this damage, which may extend only a few feet from the bearing location, the primary concern is shear failure. The research studies that focused on addressing this problem through exploring potential repair methods are relatively limited.

Fiber reinforced polymer (FRP) composites have emerged over the past two decades as an effective repair and rehabilitation material for many concrete infrastructure applications. Advantages of FRP materials over conventional steel reinforcement are their high strength to weight ratio and resistance to corrosion. The two primary FRP systems used for these applications are externally bonded laminates and near-surface mounted (NSM) bars or plates. Externally bonded systems are comprised of a fiber sheet or mat (typically glass or carbon), which is impregnated with resin to create the composite material. One method of applying the laminates to the concrete surface is through a wet layup approach, in which the resin serves to both saturate the fibers and bind the sheet to the concrete surface at the same time. Another approach is to glue pre-cured laminates to the concrete surface using resin. One disadvantage to this method is that it can only be used in situations with flat geometries, since the rigidity of a pre-cured laminate prevents it from being bent around corners.

Use of externally bonded FRP laminate systems for repair and strengthening of concrete bridge infrastructure has been largely focused on flexural applications thus far. More recently, externally bonded laminates have been used to strengthen beams in shear by way of U-wraps or bonded face plies, but effectiveness of these systems is limited by a delamination failure mode, which occurs at strains much lower than the ultimate strains achievable by the FRP composite materials themselves (ACI 440 2008). In the particular problem investigated in this study, the localization of damage necessitates a concentration of FRP material near the beam ends. Due to the presence of the bearing plate, externally bonded U-wrap schemes may not even be feasible in the field; therefore, this study focuses on bonded face ply repair schemes. Since the FRP material may only extend just past the bearing area, the behavior of FRP laminate repairs when tested with a low shear span-to-depth ratio should be investigated. Previous research has concluded that the effectiveness of shear FRP reinforcement decreases as shear span-to-depth ratio decreases (Ary and Kang 2012, Belarbi *et al.* 2011), which could further limit the usefulness of shear FRP laminates in this particular application. Furthermore, while FRP composites are generally considered environmentally resistant, the bond between the FRP and concrete may be adversely affected by the exposure to high levels of water, deicing salts, and freeze/thaw cycling applied to the end regions of these concrete bridge girders. Thus, investigating the effects of long-term environmental exposure on the bond behavior of externally bonded FRP systems is of paramount importance when determining if these systems will have long term effectiveness in repairing the end regions of concrete bridge girders.

This study investigates the use of FRP composite materials as a means of repairing and retrofitting the damaged ends of prestressed concrete bridge girders. In this study, a 3D finite element (FE) model is created for the experimental shear pull off testing previously performed on unaged and aged carbon FRP (CFRP) externally bonded laminate specimens, and the bond-slip behavior is calibrated to the experimental data. This model is utilized in a 3D FE analysis of a full scale PC bridge girder to study the effectiveness of various types of externally bonded CFRP laminate shear repairs at the damaged end regions of PC bridge girders. In addition to modelling the CFRP laminate repairs, the effect on strength and stiffness of the girder due to end region damage is investigated. Finally, reductions in stiffness and bond strength due to accelerated aging are implemented into the repaired PC bridge girder model to investigate the effectiveness of CFRP laminate shear repairs at the end region after long term environmental exposure.

## 2. Shear pull off testing

To model accurately the bond-slip behavior of unaged and aged CFRP laminates, experimental shear pull off tests were performed first on CFRP laminates bonded to 89 mm×89 mm×305 mm concrete prism specimens that had undergone accelerated aging through freeze-thaw cycling in the presence of a salt water solution. The bond length of the 76 mm wide CFRP laminate sheets was varied between 101.6 mm, 152.4 mm, and 203.2 mm. These bond lengths were chosen as a range in which the effective bond length was expected to lie. The effective bond length is the length at which the failure load of a given FRP/concrete joint is achieved (Ouezdou *et al.* 2008). The average 28-day compressive strength of the concrete specimens was 44.8 MPa.

Much research on environmental aging effects on the FRP-concrete interface has been performed, but conclusions vary significantly. Columbi *et al.* (2009) conducted pull-pull debonding tests on CFRP plates and wraps subjected to 100 and 200 freeze-thaw cycles and concluded that the conditioning did not significantly affect the ultimate load. Silva *et al.* (2014) subjected reinforced concrete beams with CFRP and glass FRP (GFRP) laminate systems to salt fog and wet-dry cycles for 10,000 hours. Salt fog cycles were more detrimental than moisture cycles for either CFRP or GFRP, and in the case of GFRP the external load capacity was actually increased after the moisture cycling. Davalos *et al.* (2008) investigated the fracture energy behavior of GFRP-concrete interfaces subjected to freeze-thaw cycling in the presence of a 4% $CaCl_2$ solution. This aging protocol resulted in fracture energy decreases of 38.5%, 50.5%, and 59% for normal strength concrete specimens at 100, 200, and 300 cycles, respectively. Subramaniam *et al.* (2008) conducted direct shear tests on CFRP sheets bonded to concrete and saw a 17% reduction in ultimate load and a 35% reduction in fracture energy after 300 freeze-thaw cycles. Al-Mahmoud *et al.* (2014) performed hinged beam tests with CFRP sheets and plates subjected to either 300 freeze-thaw cycles or 120 days of salt water immersion. The freeze-thaw cycles caused a 25% decrease in ultimate force for both the sheets and plates, while the salt water caused a deterioration of 48% for the sheets but negligible change in the plate specimens. Salt water immersion also changed the failure mode of the interface from debonding in a thin concrete layer to failure at the concrete/resin interface.

The wide range of testing setups, materials used, aging protocols, and failure modes observed in the literature make it difficult to definitively characterize the effects of long term aging on the FRP-concrete interface. Furthermore, how reductions in ultimate bond stress and fracture energy in a simple shear pull off test relate to reductions in the performance of a full scale girder with FRP laminate shear reinforcement is important to consider. To incorporate the effect of aging in the pull off tests carried out in this study, an aging protocol similar to that of Davalos *et al.* (2008) was applied. This protocol combined aspects of ASTM C666 (2015) and ASTM C672 (2012). Specimens were placed laminate side down in trays containing 6 mm of solution with a concentration of 4.21 g/100 ml of NaCl. One freeze thaw cycle was performed per day ranging from -18 to 4°C. This aggressive protocol was intended to mimic the potentially extreme conditions where deicing salts leak onto the end regions of bridge beams and multiple freezing/thawing cycles occur during the winter season. After 40 cycles, the concrete specimens showed some significant scaling, so the accelerated aging was halted and the aged specimens were tested. Fig. 1 shows an aged CFRP specimen and the test setup used for the pull off tests. The load applied at the gripped end and slip at the free end of the FRP were measured for all experimental tests. A summary of the peak loads for the 6 tests performed on unaged and aged CFRP specimens with various bond lengths is shown in Fig. 2. The accelerated aging caused an approximately 26% drop in peak load from each unaged specimen to its corresponding aged specimen.
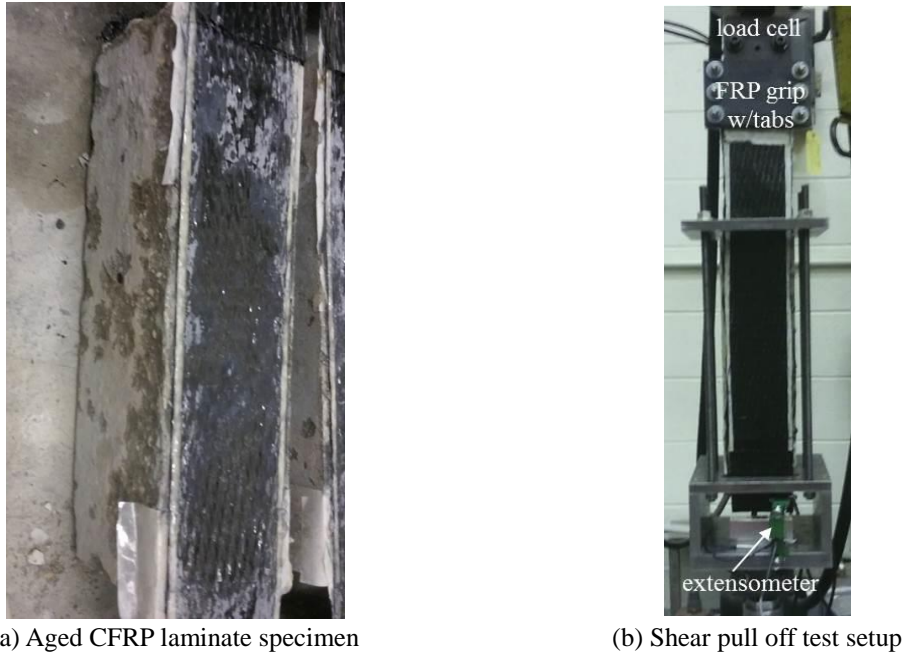
(a) Aged CFRP laminate specimen                    (b) Shear pull off test setup

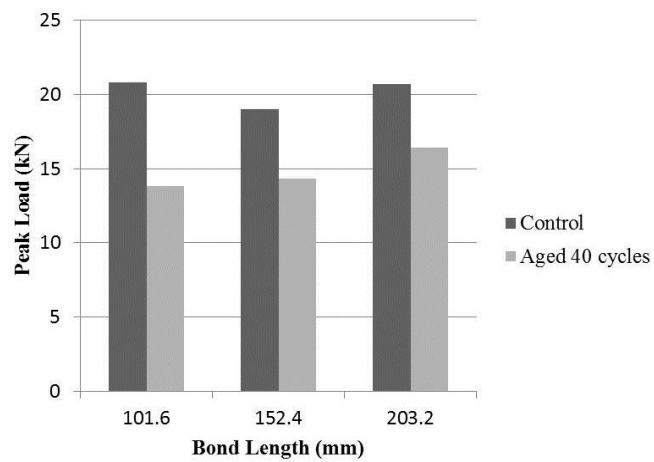Fig. 1 CFRP laminate specimen after accelerated aging and shear test setup



Fig. 2 Peak loads for CFRP laminate specimens

## 3. Bond-slip finite element modeling

All finite element modeling in this study was performed using the software program ABAQUS/CAE 6.13 (Dassault Systèmes 2013). Each model of the pull off tests discussed in the previous section was comprised of three geometrical components: a concrete prism, an FRP laminate, and a thin cohesive interface layer between the concrete and the FRP laminate.
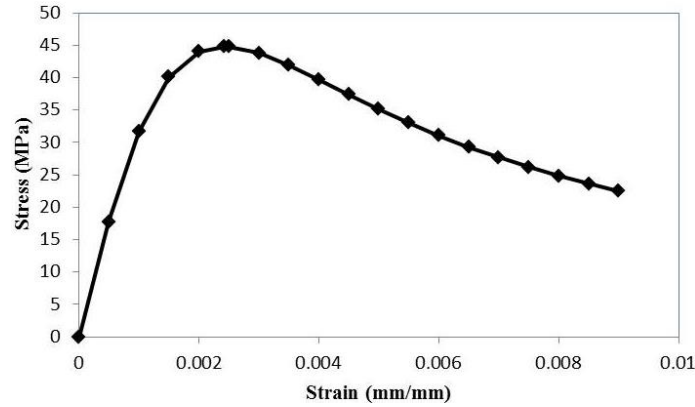
### 3.1 Concrete block

Fig. 3 Concrete compressive stress-strain behavior

The 89 mm×89 mm×305 mm concrete prism was modeled using C3D8 8-node linear brick elements. The eight nodes defining each brick element are each associated with three translational degrees of freedom. The concrete material model consisted of an isotropic linear elastic ascending branch, followed by plastic behavior defined through the concrete damaged plasticity model parameters. The concrete modulus of elasticity $E_c$ was calculated as $4.73\sqrt{f'_c}$, or 31.7 GPa. The compressive behavior was based on Todeschini (1964) stress-strain model shown in Eq. (1). The strain at maximum compressive stress is calculated using Eq. (2) (MacGregor and Wight 2005), where $f_c$ is concrete stress at any given strain $\varepsilon$ and $\varepsilon_o$ is strain at maximum compressive strength $f'_c$. The stress-strain curve used in this analysis is shown in Fig. 3.

$$f_c = \frac{2f'_c\left(\dfrac{\varepsilon}{\varepsilon_o}\right)}{1+\left(\dfrac{\varepsilon}{\varepsilon_o}\right)^2} \tag{1}$$

$$\varepsilon_o = \frac{1.71f'_c}{E_c} \tag{2}$$

The tensile behavior of concrete is defined by a linear ascending branch up to the modulus of rupture (taken as $0.622\sqrt{f'_c}$, or 4.17 MPa), followed by a descending linear branch, as seen in Fig. 4. If a realistic value for strain at the end of the descending branch is used in the tension model, convergence issues may occur. Therefore, the value for ultimate strain is typically specified as the lowest value that will allow for convergence of the model, shown as 0.0005 in Fig. 4.

### 3.2 FRP laminate

The FRP laminate sheets were modeled using S4 4-node linear shell elements. Orthotropic plane stress linear elastic behavior was used to define the FRP material, which requires parameters $E_1$, $E_2$, $\nu_{12}$, $G_{12}$, $G_{13}$, and $G_{23}$. The properties of the unidirectional carbon fiber composite and epoxy matrix were taken from the manufacturer's data (QuakeWrap 2016a, b). The specified $E_1$
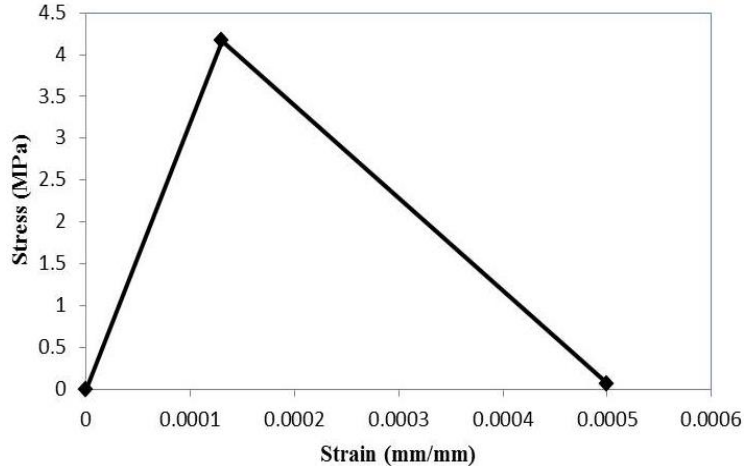
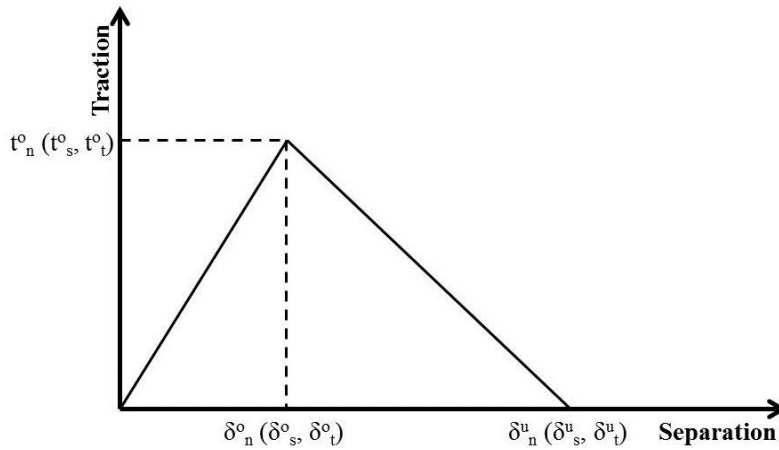Fig. 4 Concrete tensile stress-strain behavior



Fig. 5 Typical traction-separation behavior for cohesive elements (Dassault Systèmes 2013)

and $E_2$ correspond to the elastic moduli in the longitudinal (parallel to fibers) and transverse (perpendicular to fibers) directions in the laminate. $E_1$ was defined as 89.6 GPa (elastic modulus of carbon fibers laminated with epoxy resin), while $E_2$ was defined as 2.0 GPa (the elastic modulus of the epoxy resin only). The Poisson's ratio and shear moduli were not provided by the manufacturer, so values were estimated. The volume fraction of fibers, $V_f$, was calculated as 0.383 using Eq. (3) and the known elastic moduli for the carbon fibers ($E_f$=231 GPa), epoxy matrix ($E_m$=2.0 GPa), and resulting composite laminate ($E$=89.6 GPa).

$$E = (1 - V_f)E_m + V_f E_f \tag{3}$$

Using the charts for carbon/epoxy composites in Younes *et al.* (2012), the values for $\nu_{12}$, $G_{12}$, $G_{13}$, and $G_{23}$ were approximated as 0.32, 4.1 GPa, 4.1 GPa, and 2.8 GPa, respectively. The composite layup tool was used to assign and appropriately orient the material properties to the laminate part and specify a thickness of 1.24 mm.

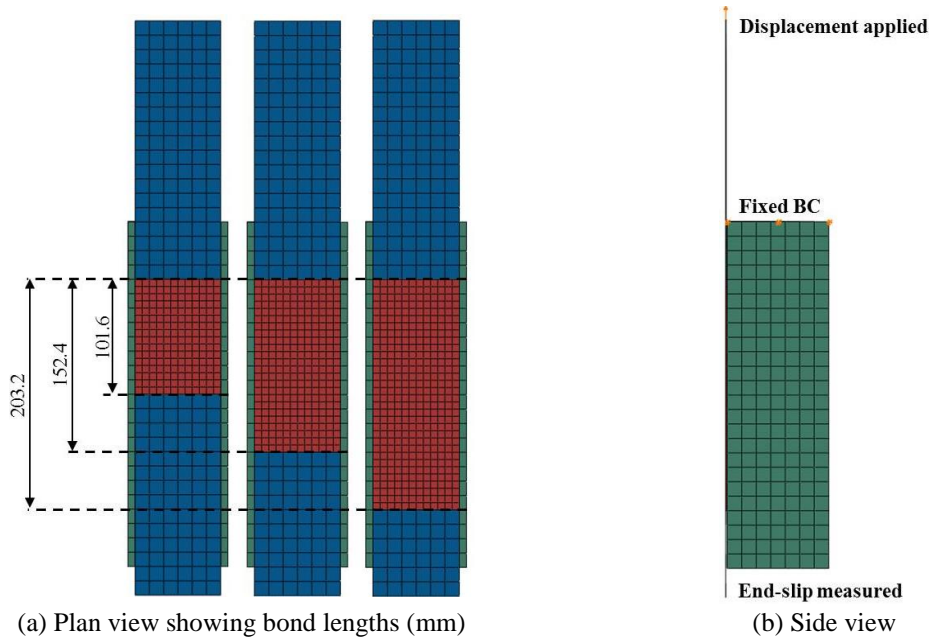(a) Plan view showing bond lengths (mm)                    (b) Side view

Fig. 6 Shear pull off models with varying bond lengths

### 3.3 Cohesive interface

When modelling FRP composites bonded to concrete, it is crucial to include some sort of cohesive interaction or interface between the two substrates in order to accurately model the delamination/debonding failure mode that is often prevalent in this application. For this model, a thin layer was placed between the FRP laminate and concrete block, meshed with COH3D8 8-node three-dimensional cohesive elements. The cohesive behavior was modeled through a traction-separation response. The traction-separation behavior consists of a linear ascending branch, damage initiation, and damage evolution, seen in Fig. 5.

Once the stresses at a node reach the damage initiation criteria, degradation begins. The damage initiation criteria used was the maximum nominal stress criterion, in which damage initiates when any of the maximum stress values assigned are reached. Three maximum stress values were prescribed; normal to the interface, and shear in the first or second directions. The maximum normal stress value was chosen as the modulus of rupture of concrete (4.17 MPa), which represents the delamination failure mode that is caused by concrete cracking and occurs just below the surface of the concrete substrate. The maximum shear stresses were calibrated based upon the results from the experimental testing. In addition to the damage initiation criteria, uncoupled traction-separation moduli were assigned ($E_{nn}$, $E_{ss}$, $E_{tt}$). These values relate the nominal strains in the cohesive layer to the traction vector through the elasticity matrix (Eq. (4)). The nominal strains are a function of the corresponding separations in the normal or either shear direction ($\delta_i$) and the initial thickness of the cohesive layer ($T_o$) (Eq. (5)). The uncoupled traction-separation moduli was adjusted during the calibration process to achieve a good fit with the experimental data. The damage evolution used in this model is characterized by a linear branch from the point of damage initiation to zero stress at a specified failure displacement, another

parameter that was adjusted during the calibration process.

$$t = \begin{Bmatrix} t_n \\ t_s \\ t_t \end{Bmatrix} = \begin{bmatrix} E_{nn} & 0 & 0 \\ 0 & E_{ss} & 0 \\ 0 & 0 & E_{tt} \end{bmatrix} \begin{Bmatrix} \varepsilon_n \\ \varepsilon_s \\ \varepsilon_t \end{Bmatrix} \tag{4}$$

$$\varepsilon_i = \frac{\delta_i}{T_o} \tag{5}$$

### 3.4 Model assembly

Tie constraints were used to affix either side of the cohesive layer to the concrete block and FRP laminate. Tie constraints tie separate surfaces together so that there is no relative motion between them and allows surfaces with dissimilar meshes to be connected. A node to surface discretization method generates tie coefficients according to the interpolation functions at the points where slave nodes project onto the master surface (Dassault Systèmes 2013). A finer mesh was generated on the cohesive layer, as this was the slave surface when applying the tie constraints to the concrete and FRP laminate. The length of the cohesive layer was varied between 101.6 mm, 152.4 mm, and 203.2 mm to model each of the tested experimental bond lengths. Displacement was applied at top end of the laminate, while end-slip was measured at the opposite end. A fixed boundary condition was applied to the top of the concrete block on the end where displacement was applied. Fig. 6 shows several of these model assemblies.

### 3.5 Model calibration

In order to represent the experimental results, several parameters of the cohesive element layer had to be calibrated, namely the traction-separation moduli ($E_{nn}$, $E_{ss}$, $E_{tt}$), maximum bond shear stresses ($\tau_1$, $\tau_2$), and displacement at failure ($\delta_u$). The calibration process involved several iterations, after each of which the force vs. end-slip behavior was plotted and compared to that of the experimental results. The interface stiffness was assumed isotropic, so all three traction-separation moduli were calibrated with a single value $E$. Likewise, the maximum bond shear stress in either direction was set to the same value $\tau_{max}$. It was not possible to create a single set of parameters that would accurately predict the force-slip behavior for all bond lengths tested; thus, each bond length model was calibrated to its respective experimental test to create a set of cohesive element properties. The same process was repeated and compared to the experimental force-slip curves of the CFRP laminate specimens that had been aged for 40 cycles. Table 1 summarizes these calibrated parameters for the unaged and aged CFRP specimens. The reductions in stiffness ($E$) and strength ($\tau_{max}$) of each bond length between the aged specimens and their respective unaged specimens were calculated and averaged together, as shown in Table 1. Fig. 7 compares the force-slip curves generated from the model calibration with those obtained experimentally for the unaged and aged specimens for the intermediate bond length (152.4 mm). Because the simplified bilinear bond-slip model used in the analysis cannot account for the nonlinear behavior observed experimentally for some of the specimens, all models were calibrated to the initial stiffness of the FRP-concrete joint, up to the point of maximum force for each individual test.

Table 1 Calibrated cohesive layer parameters

| Model | $\tau_{max}$ (MPa) | $\tau_{max}$ reduction | $E$ (MPa) | $E$ reduction |
|---|---|---|---|---|
| C1[*]-Unaged | 3.09 | -- | 100.0 | -- |
| C1-Aged | 1.93 | 37.5% | 58.6 | 51.2% |
| C2-Unaged | 2.04 | -- | 94.5 | -- |
| C2-Aged | 1.43 | 29.7% | 55.2 | 41.4% |
| C3-Unaged | 1.90 | -- | 147.3 | -- |
| C3-Aged | 1.35 | 29.0% | 81.6 | 41.6% |
| Avg. Reduction | -- | 32.1% | -- | 44.7% |

*C1: bond length of 101.6 mm; C2: bond length of 152.4 mm; C3: bond length of 203.2 mm



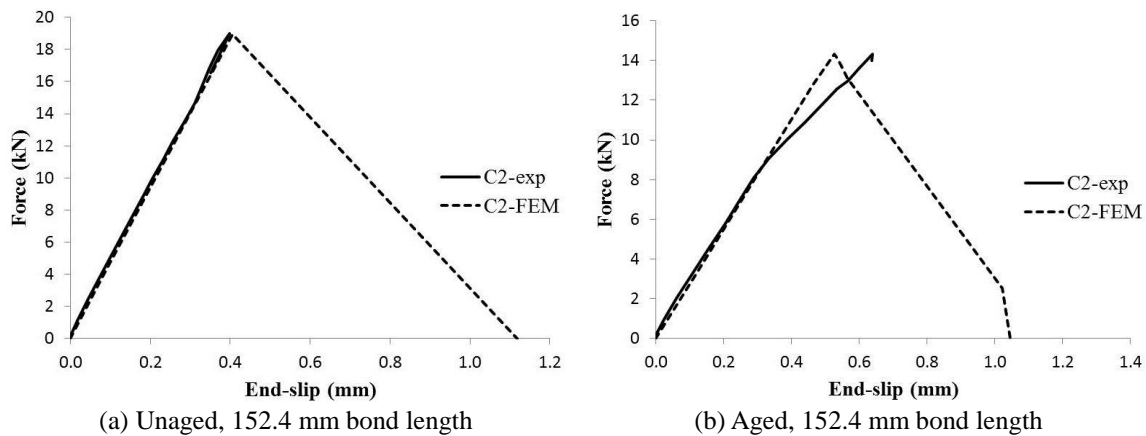(a) Unaged, 152.4 mm bond length          (b) Aged, 152.4 mm bond length

Fig. 7 Force vs. end-slip of CFRP laminate shear pull off experimental tests and calibrated FEM models

## 4. PC I-girder finite element model

### 4.1 Model description and verification

The model of the prestressed concrete (PC) I-girder analyzed in this study was based on experimental tests performed by Andrawes and Pozolo (2011). The I-girder model included several geometrical parts: high strength steel prestressed strands, mild steel bars and stirrups, the concrete girder, and loading/support plates. To reduce computational demand, half of the I-girder cross-section is modeled, with a symmetric boundary condition placed on the inner face of the girder.

### 4.2 Prestressing strands and mild steel

The prestressing strands and mild steel bars and stirrups were modeled using T3D2 2-node linear 3-D truss elements. These elements consider tension and compression, but not bending. Each node is associated with three translational degrees of freedom. The prestressing strands have a cross-sectional area of 98.7 mm$^2$, elastic modulus of 197.9 GPa and ultimate strength of 1862 MPa. The nonlinear stress-strain curve is a simplified version of that typically seen with high strength prestressing strands, with yielding occurring at 90% of the ultimate strength, or 1675 MPa

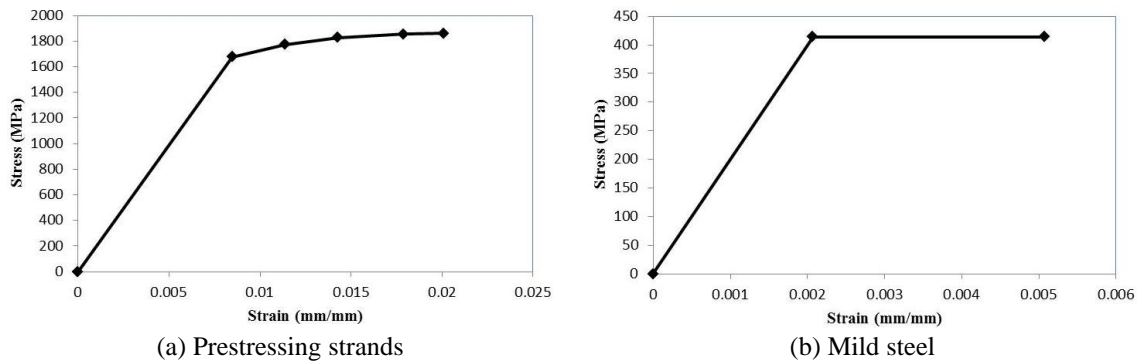(a) Prestressing strands                    (b) Mild steel

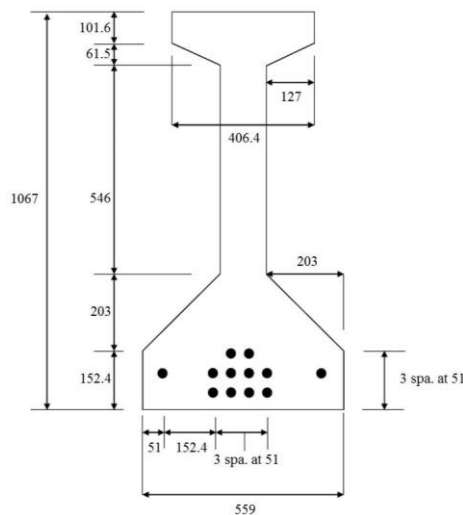Fig. 8 Stress-strain curves for steel used in PC I-girder model



Fig. 9 Cross-sectional dimensions of I-girder (Andrawes and Pozolo 2011), in mm

(Fig. 8). Prestress was applied by imposing a negative predefined temperature field on the strands, which have been given a thermal expansion coefficient, to create tension in the strands. This tension is transferred to the concrete in the first step of the analysis, inducing camber in the girder. The thermal expansion coefficient was adjusted until the effective prestress after transfer is at approximately 1140 MPa. Mild steel was modeled as elastic-perfectly plastic with an elastic modulus of 200 GPa and a yield strength of 413.7 MPa (Fig. 8). Exact size and location of longitudinal bars and stirrups can be found in Andrawes and Pozolo (2011). All of the mild and prestressing steel was embedded within the concrete girder. The translational degrees of freedom of the nodes of embedded elements are constrained to the interpolated values of the corresponding degrees of freedom of the host element (Dassault Systèmes 2013).

### 4.3 Concrete girder

The same element type and material models for compressive and tensile behavior that were used in the pull off test were used for the I-girder. Fig. 9 shows the cross-sectional dimensions of

(a) Three point bending test setup



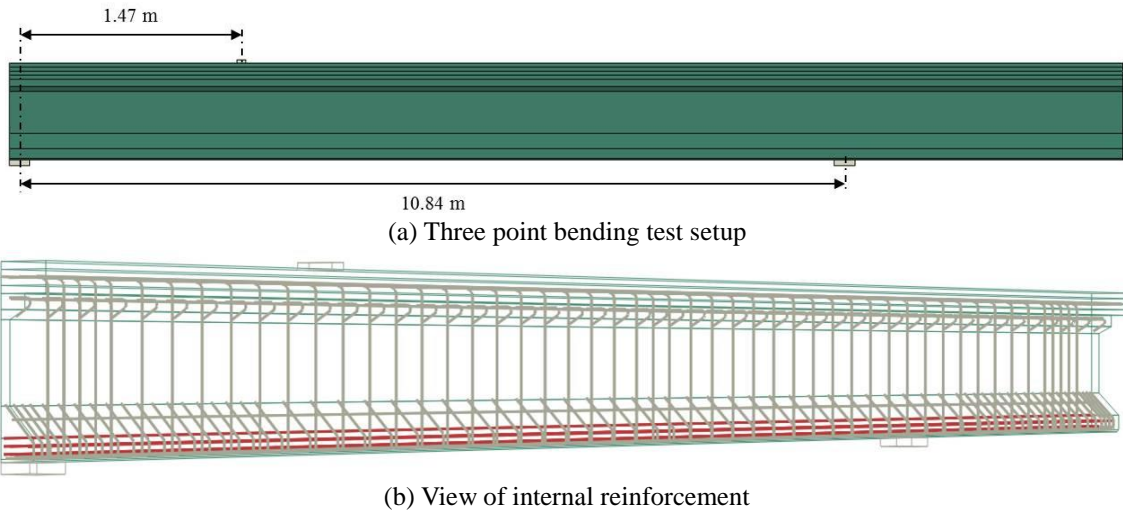(b) View of internal reinforcement

Fig. 10 Model assembly for three point bending calibration

the girder (without the added slab) and the layout of the prestressing strands. The girder measures 14.63 m in length. The concrete compressive strength $f'_c$ was specified as 41.8 MPa, which is 90% of the $f'_c$ of I-Girder 2 as tested in Andrawes and Pozolo (2011). The 10% reduction in compressive strength accounts for the difference between cylinder and member strength. The 203 mm×762 mm slab portion that was cast on top of the I-girder was assumed to have the same compressive strength. While in practice the deck slab would likely have a lower compressive strength, this was not necessary to calibrate since the model performs similarly to that in Andrawes and Pozolo (2011). Additionally, the strength of the deck has little to no effect on the CFRP-concrete bond for shear CFRP reinforcement. To account for the casting of the slab after transfer of prestress, a positive predefined temperature field is applied to the slab portion of the model and the longitudinal rebar contained within the slab portion. This creates compression in the slab, which counteracts the tension produced in the slab by the cambering of the girder in the prestressing step.

### 4.4 Loading and support plates

The loading and support plates used the same material model as the mild steel, but with C3D8 8-node linear brick elements. The exact width and depth of the support plates and loading plate used in Andrawes and Pozolo (2011) were used in this model in order to recreate boundary conditions as close as possible to the experimental test. The supports were tied to the concrete surface on one face, and boundary conditions representing either a pin or roller were applied along the center line of the opposite face of the plate. The same concept was applied to the loading plate, but with a downward displacement along the center line of the plate instead of a boundary condition.

### 4.5 Model verification

Before performing damage and CFRP repair studies on the I-girder, it was necessary to first verify the model with the experimental data. The loading plate and support locations were placed in the three-point
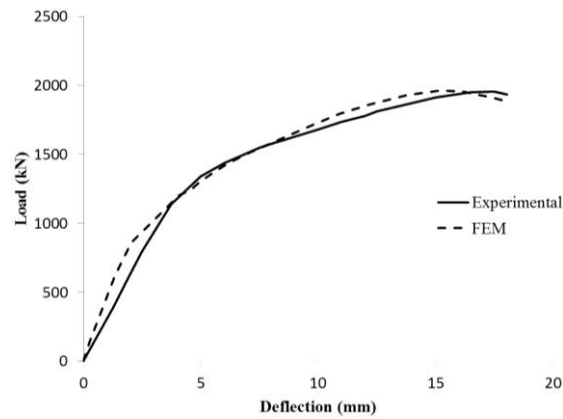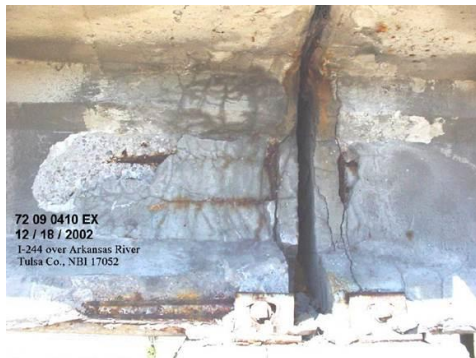
Fig. 11 Load-deflection plots for model calibration to Andrawes and Pozolo (2011)



| (a) End damage of girder | (b) Typical mortar repair of girder end |

Fig. 12 End region damage and mortar repair of concrete bridge girder

loading position of Test 7 (Andrawes and Pozolo 2011), which has a shear span of 1.47 m and a support to support distance of 10.84 m. Fig. 10 shows the model assembly in this test configuration. Deflection was measured under the point of loading, and the load-deflection curve obtained from analysis was compared to that from the test (Fig. 11). While the initial stiffness of the FEM model is slightly greater than the experimental test, the load-deflection behavior correlates reasonably well overall.

## 5. Damage and mortar repair analysis

After verifying the I-girder model, the effect of end region damage was investigated. The goal of this portion of the study was to apply damage to the model in a way that was representative of the type of end region damage that could be expected in the field, and compare the behavior of the damaged beam with that of the control. In addition to investigating the effect of damage, the recovery effect of a mortar repair on the damaged end region, which is a common repair technique used in the field, is explored. Fig. 12 shows an example of the type of end region damage that could be expected in the field as well as a typical mortar repair of a damaged beam end. Since this damage occurs at the location of expansion joints, it can occur over piers (Fig. 12(a)) or at locations of exterior bearing (Fig. 12(b)).

(a) Cover damage profile                          (b) Cover damage zones



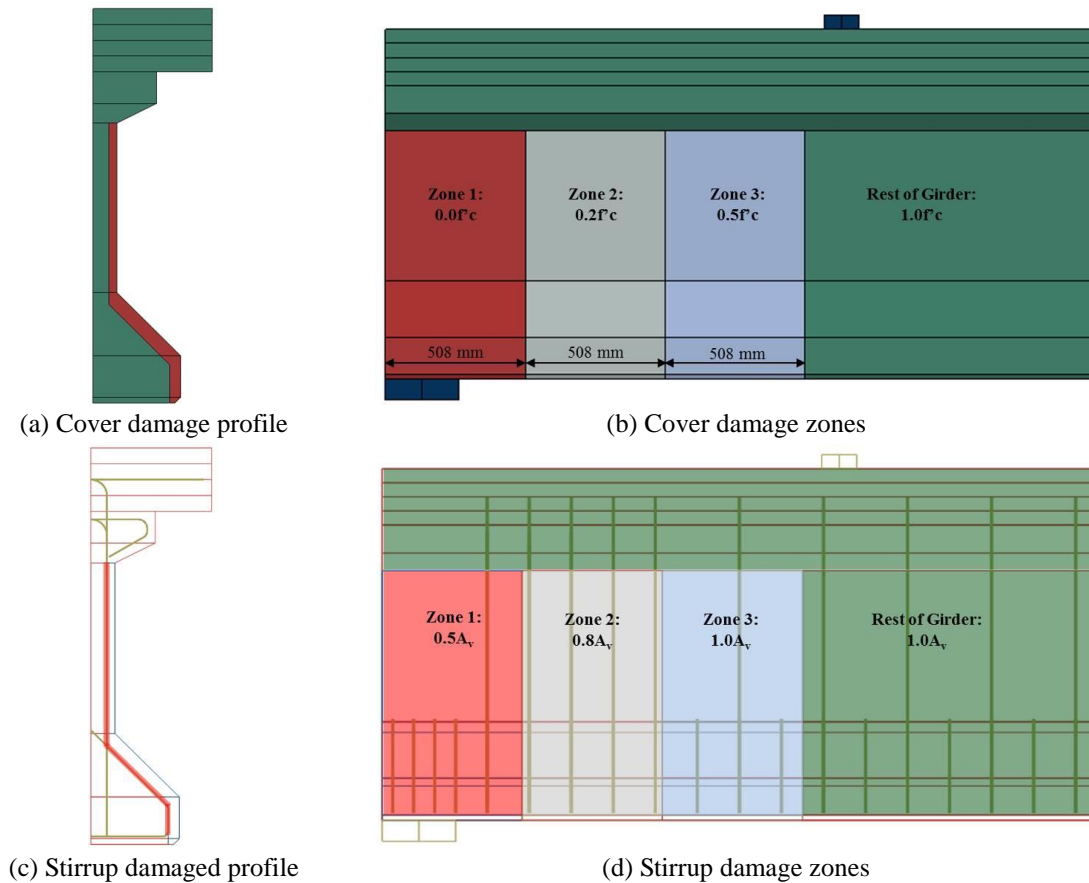(c) Stirrup damaged profile                       (d) Stirrup damage zones

Fig. 13 Progressive end region damage scheme

Because of the localized nature of the end region damage, shear failure is the primary concern. While bridge girders are typically designed for sectional shear, end region damage may not affect the sectional shear capacity of the girder. Since the damage may not progress much more than the beam depth from the end, the behavior of the beam in a short shear span test should be investigated. This will ensure shear cracking occurs within the damaged region. For this reason, the shear span was chosen as 1.3 of the beam depth, or 1.52 m, for all the I-girder models performed in this section and beyond. The supports were placed at the ends of the girder, to represent the configuration used in the field of a simply supported beam with no cantilever.

The end region damage observed in the field largely affects the cover concrete of the girder. In severe cases, the stirrups may be corroded, and the cover concrete can be completely spalled off. These ideas were applied to the model to create a case where damage has progressed to the point of concrete cover loss at the very end of the beam with corrosion occurring in the outermost portions of the stirrups. The idea of damage progression starting from the end of the girder is taken into account by partitioning the damaged region into three 508 mm wide zones, and prescribing different levels of damage to each zone. In Zone 1 (closest to the end), the compressive strength of cover concrete is reduced to $0.0\,f'_c$ and the area of the stirrups is reduced to $0.5\,A_v$, where $A_v$ is the undamaged cross-sectional area of the stirrups. In Zone 2, the compressive strength of cover concrete is reduced to $0.2\,f'_c$ and the area of the stirrups is reduced to
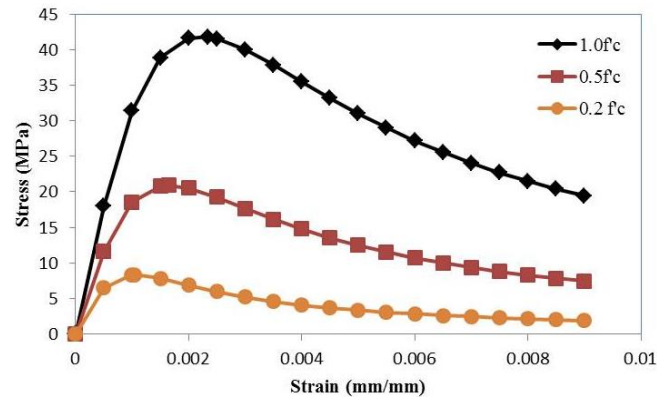
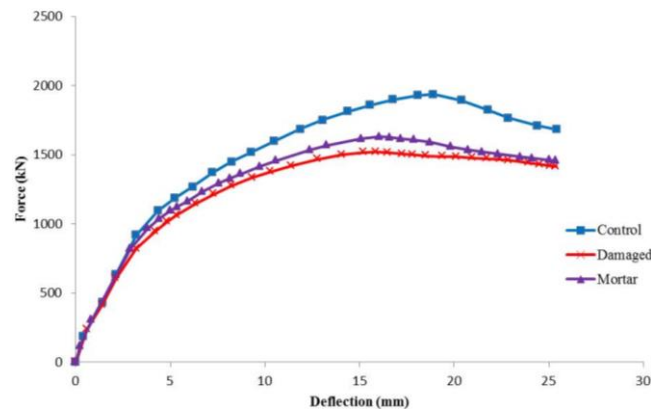Fig. 14 Reduced strength cover concrete stress-strain curves



Fig. 15 Load-deflection plots for control, damaged, and mortar repaired girder

0.8 $A_v$. In Zone 3, the compressive strength of cover concrete is reduced to 0.5 $f'_c$ and the area of the stirrups is left at 1.0 $A_v$. The length of these zones was determined by dividing the shear span into three even sections. Fig. 13 illustrates this progressive damage scheme. Fig. 14 shows the reduced compressive strength stress-strain curves for the cover concrete. For Zone 1, the cover concrete was given an elastic modulus close to zero so that this concrete would provide negligible force resistance.

Next, a model was created to represent a typical mortar repair to the damaged end region of the girder. High strength repair mortars can achieve strengths in excess of 50 MPa, but early set strengths tend to be in the range of 20-30 MPa. The cold joint that exists between the mortar repair and existing concrete may also limit the ability of the mortar to contribute to the shear strength of the girder. For these reasons, the mortar strength was approximated as 20.9 MPa for the purposes of this study. In this model, the cover concrete strength in Zones 1 and 2 is increased to 20.9 MPa (or 0.5 $f'_c$) and Zone 3 is left at 0.5 $f'_c$. The reduced area stirrups in Zones 1 and 2 are left as is to represent a scenario in which mortar is placed over the corroded stirrups without additional steel reinforcement being provided. Fig. 15 shows the load-deflection plots for the control, damaged, and mortar repaired I-girder models. The damaged case resulted in a 21.5% decrease in strength and 17% loss in stiffness compared to the control. Secant stiffnesses are compared at the onset of nonlinear behavior at a deflection of approximately 4 mm. The mortar repaired case saw a 15.8% decrease in strength from the control (recovered 5.7%), but stiffness recovery was
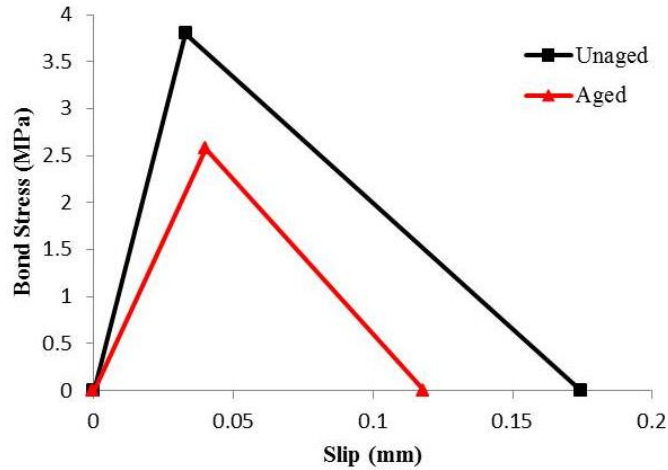
Fig. 16 Bond stress-slip model used for FRP/concrete interface

negligible. This study shows that supplementary reinforcement, in addition to a basic mortar repair, is necessary to regain the capacity of the control girder. It is important to note that due to the short shear span-to-depth ratio investigated in this study, failure of the girder occurs due to arch action, not conventional beam action shear failure.

## 6. CFRP laminate repair analysis

After concluding that a mortar repair alone is insufficient to regain the original strength and stiffness of the I-girder, CFRP laminate repair studies were conducted. Rather than using the calibrated parameters from the bond-slip tests in Section 2, an appropriate cohesive bond stress-slip model was chosen from the literature. This would ensure that the CFRP/concrete interface modelled is representative of an average of experimental tests conducted by various researchers and not just the results of one set of tests. Lu *et al.* (2005) proposed three bond stress-slip models based on a database of existing pull tests. These models, particularly the bilinear model, have been used in many FE analyses to exhibit the debonding failure at the FRP/concrete interface. One drawback to the Lu bilinear model is the difficulty in interpreting a geometrical constant that relates the width of the FRP laminate to the width of the concrete prism to which it is attached. For shear FRP applications, this value cannot be easily determined. Sato and Vecchio (2003) proposed a similar bilinear model that solely depends on the concrete strength and assumes failure within the thin layer of concrete below the FRP/concrete interface. This model has been validated in FE analyses of shear FRP reinforced PC girders by both You *et al.* (2011) and Qapo *et al.* (2014). Therefore, this model was chosen to model the FRP/concrete interface. Eqs. (6)-(9) define the bilinear bond-slip curve used in this study, where $\tau_{max}$ is the maximum bond stress, $S_o$ is the slip at $\tau_{max}$, $S_u$ is the ultimate slip, and $G_f$ is the fracture energy.

$$\tau_{\max} = (54f'_c)^{0.19} \text{(MPa)} \tag{6}$$

$$S_o = 0.057\sqrt{G_f} \text{ (mm)} \tag{7}$$

Table 2 Test matrix for all parametric series

| Model | Plies # | Width of CFRP Laminate (mm) | Long. CFRP Web Anchors | Peak Load (kN) | % of control |
|-------|---------|------------------------------|------------------------|----------------|--------------|
| P1-1 | 1 | 508 | -- | 1702.2 | 87.9% |
| P1-2 | 1 | 1016 | -- | 1813.6 | 93.7% |
| P1-3 | 1 | 1524 | -- | 1983.7 | 102.5% |
| P1-F | 1 | 1721 | -- | 1978.5 | 102.2% |
| P1-3-wa | 1 | 1524 | 76 mm width, 51 mm bond length at end | 2043.5 | 105.6% |
| P2-F | 2 | 1721 | -- | 2011.2 | 103.9% |
| P1-F-Aged | 1 | 1721 | -- | 1945.9 | 100.5% |



(a) P1-1 (Zone 1)



(b) P1-2 (Zones 1-2)



(c) P1-3 (Zones 1-3)
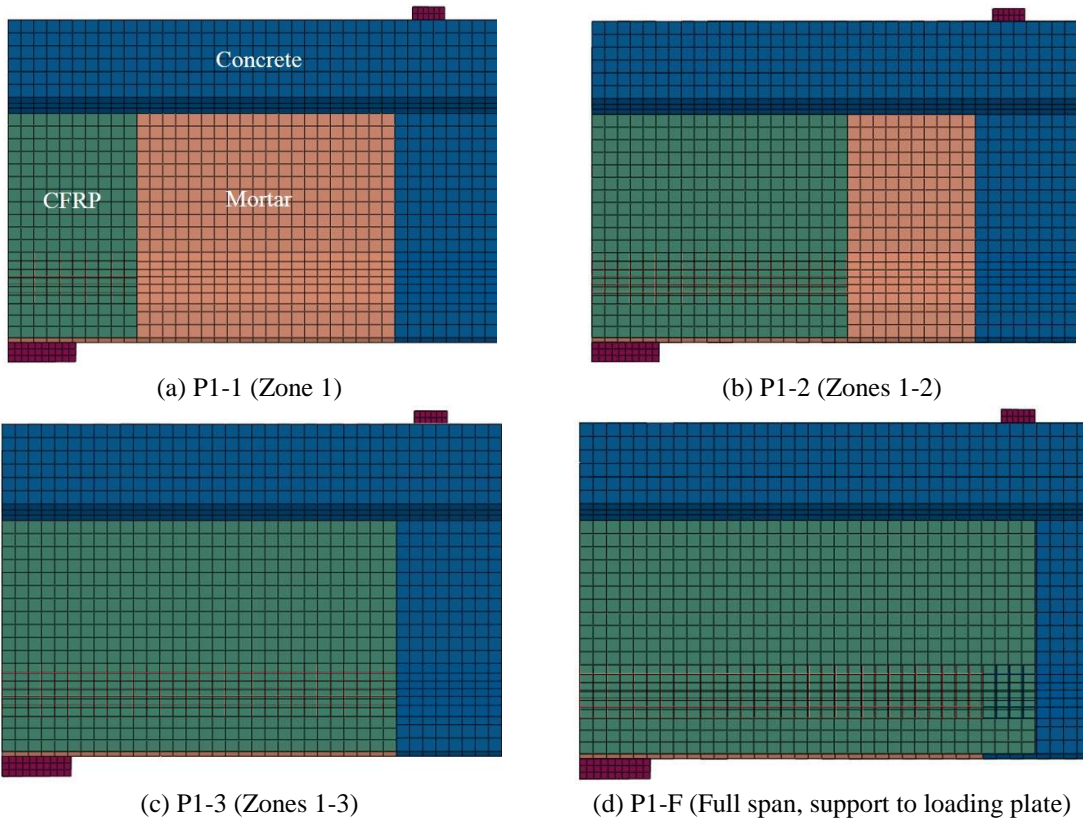


(d) P1-F (Full span, support to loading plate)

Fig. 17 Extent of CFRP shear reinforcement in P1-1 through P1-F models

$$S_u = \frac{2G_f}{\tau_{max}} \ \text{(mm)} \tag{8}$$

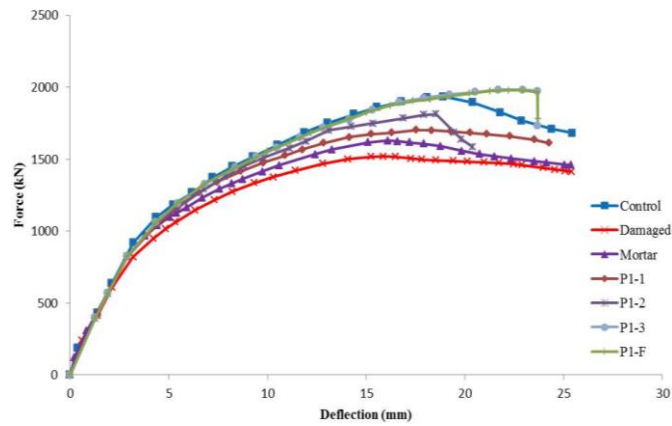$$G_f = \left(\frac{\tau_{max}}{6.6}\right)^2 \ \text{(N/mm)} \tag{9}$$

Fig. 18 Effect of FRP reinforcement on load-deflection response of P1-1 through P1-F models



(a) P1-1                    (b) P1-2
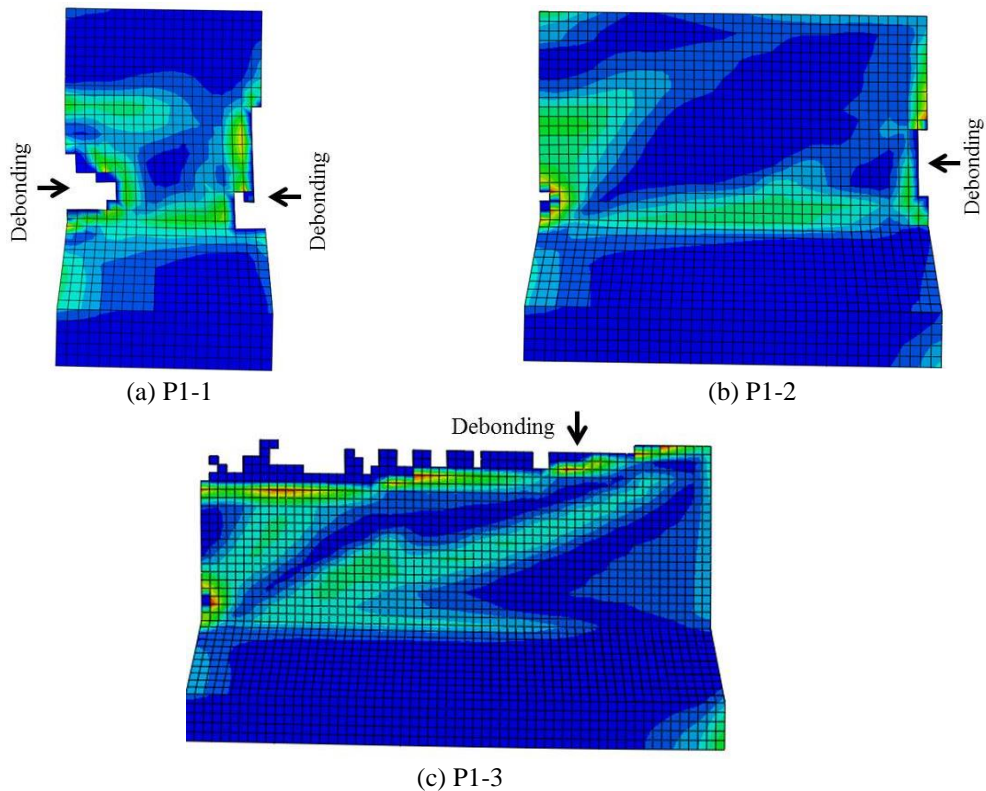


(c) P1-3

Fig. 19 Cohesive interface debonding (region of debonding onset indicated)

The $f'_c$ was chosen as 20.9 MPa, the assumed strength of the cover concrete after mortar repair. To incorporate the effect of accelerated aging, the average reductions in the maximum bond stress and stiffness of the interface from Table 1 are applied to the Sato and Vecchio model to generate an aged bond stress-slip curve. The unaged and aged bond stress-slip models used in this study are shown in Fig. 16.

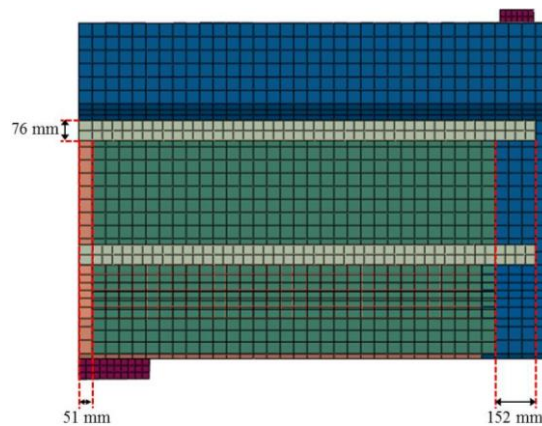The goal of this portion of the study was to determine if CFRP laminates could be effective in

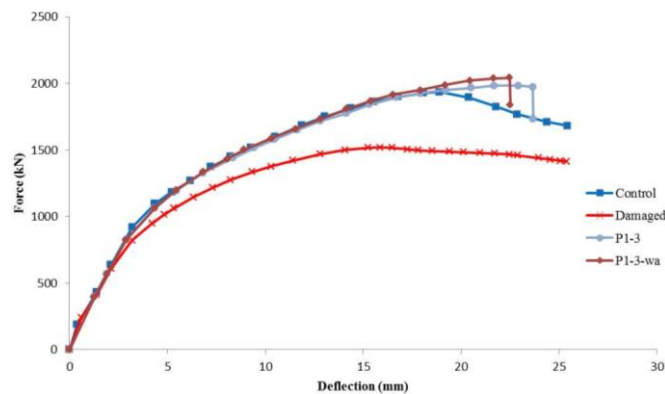Fig. 20 Parametric Series 2: Web anchor effect (P1-3-wa)



Fig. 21 Effect of adding web anchorage on load-deflection response

restoring the original capacity of the girder when tested at a low shear span to depth ratio (1.3), then investigate different web anchoring schemes using longitudinal CFRP laminates to determine the most efficient and effective use of material for this application. All the models run in these parametric series are summarized in Table 2.

The first four models in the parametric series (P1-1, P1-2, P1-3, and P1-F) used 1 ply of unidirectional CFRP oriented vertically as shear reinforcement with no web anchorage and with varying extent of coverage from the end of the beam. The purpose of this series is to determine how much of the damaged end region is necessary to be repaired with CFRP. Fig. 17 shows the various CFRP layouts of this series. The load-deflection plots for this series are shown in Fig. 18.

P1-3 and P1-F were able to recover the stiffness of the control girder and achieved peak loads of 102.5% and 102.2%, respectively, of that of the control before debonding of the CFRP occurred. Fig. 19 shows the stress contours of the cohesive interface at the moment of debonding for P1-1, P1-2, and P1-3. The onset of debonding in P1-1 and P1-2 occurs on the right side of the CFRP sheet due to tensile cracking in the web coinciding with the termination point of the laminate. Debonding also occurs subsequently at the left side of the CFRP sheet for P1-1 and P1-2. For the laminates that extend further, debonding initiates near the top of the laminate, where tensile cracking in the web meets the top flange of the girder. For all cases, there is also a stress concentration located at the web/bottom flange junction on
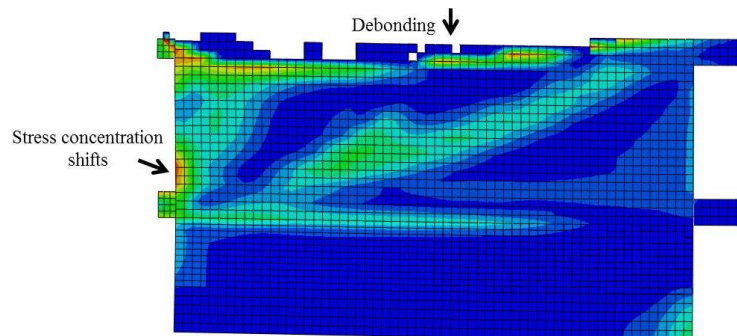
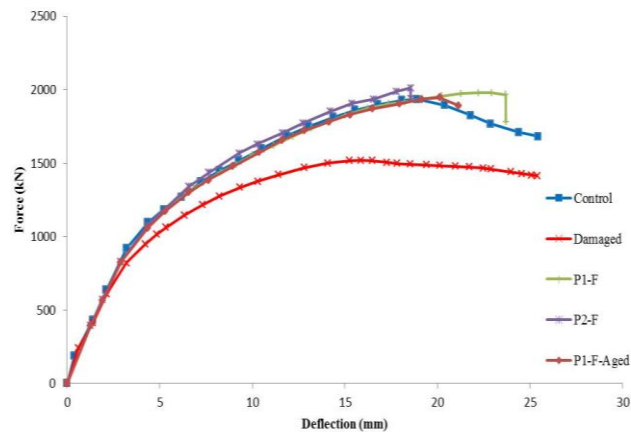Fig. 22 Cohesive interface debonding (P1-3-wa)



Fig. 23 Effects of FRP thickness and aging on load-deflection response

the left side of the laminate. This stress concentration, as well as the debonding at the top of the laminate, are addressed in the next study with the introduction of longitudinal CFRP web anchors.

Next, the effect of using longitudinal web anchors at the top and bottom of the web was studied in the P1-3-wa model in an attempt to delay debonding and improve the effectiveness of the shear CFRP laminates. In this model, 76 mm wide longitudinal CFRP anchors are placed at the top and bottom of the web. In order to develop the CFRP anchors, some bonded area to the concrete is needed. These anchors have a 152 mm extension past the shear CFRP panel on the right side, but at the end of the beam a 51 mm bond length was prescribed, which should allow for development of the anchor at the beam end with only a minor loss of shear CFRP coverage at the very end of the beam. The amount of shear CFRP used in this model is equal to that used in P1-3. The anchors are tied to the shear CFRP where they overlap and are connected to the concrete through a cohesive layer where they extend past the shear CFRP. Fig. 20 shows this configuration. The load-deflection plot for this model is shown in Fig. 21.

The addition of longitudinal web anchors proved beneficial in increasing the peak load to 105.6% that of the control, an increase of 3.1% over P1-3. However, this small increase is likely within the expected error of this model. The stiffness did not change significantly with the addition of anchors, although debonding did occur at a slightly lower deflection than P1-3 (22.5 mm vs 23.7 mm). The debonding failure mode is similar to that of P1-3 in that it starts at the top of the shear CFRP near the middle of the shear span and proceeds towards the end of the beam (Fig. 22). However, the bottom web anchor does

somewhat relieve the stress concentration in the shear CFRP at the web/bottom flange junction near the end of the beam.

Finally the effect of increasing the FRP thickness by using 2 plies of shear CFRP as well as the effect of accelerated aging were studied. Model P2-F is identical to P1-F except that the CFRP laminate thickness is increased to 2.48 mm to represent 2 plies. The aged bond stress-slip model was applied to the model P1-F-Aged, which is otherwise identical to P1-F. The load deflection plots from these models are shown in Fig. 23.

The addition of an extra ply of CFRP slightly increased the stiffness and peak load of the girder, but with a significant decrease in ductility. This concept is noted in the ACI 440 (2008) design equations for FRP contribution to shear strength, where additional bonded face plies decrease the active bond length, which in turn decreases the effective strain of the FRP at debonding. P1-F-Aged followed the load-deflection curve of P1-F, but debonding initiated at a lower load/deflection. This model was still able to reach 100.5% of the peak load of the control girder (only 1.6% less than the unaged case), however, without a loss in member stiffness. This shows that despite the significant reduction in stiffness of the bond stress-slip model for the aged FRP/concrete interface, the global stiffness of the girder was unaffected.

## 7. Conclusions

Finite element analysis was utilized in this study to investigate the damaged end regions of PC I-girders and the effectiveness of CFRP laminate shear reinforcement repairs under a low shear span-to-depth ratio. The results of shear pull off tests on unaged and aged CFRP laminates were used to predict reduction in bond stress-slip properties of the FRP/concrete interface layer. Parametric studies were performed to determine the most effective use of externally bonded CFRP laminates to restore the capacity of a full-scale PC I-girder with a severely damaged end region. From this analysis, the following conclusions were drawn.

• A conventional mortar repair is not enough to regain the strength and stiffness of a girder with a severely damaged end region, especially if the stirrups have experienced area loss due to corrosion.

• Shear FRP should extend past the point of expected cracking in the web in order to prevent premature debonding failure of shear FRP in middle of the web. If FRP is extended far enough, debonding will initiate at the top of the web.

• Longitudinal FRP anchors at the top and bottom of the web can slightly delay debonding and help achieve higher shear strengths than with shear FRP alone. However, this slight difference is likely within the expected error inherent in this model.

• In the case of a low shear span-to-depth ratio, addition of more plies of FRP may not be an economical or effective use of material. It can severely reduce the ductility of the FRP/concrete joint for relatively minor gains in strength and stiffness of the member.

• Even after a 32.1% reduction in the peak bond stress and 44.7% reduction in stiffness of the FRP/concrete interface due to environmental aging, externally bonded CFRP laminates could regain the original stiffness and load capacity of the PC I-girder with a severely damaged end region.

## References

ACI 440 (2008), *Guide for the Design and Construction of Externally Bonded FRP Systems for Strengthening Concrete Structures*, Michigan, U.S.A.

Al-Mahmoud, F., Mechling, J. and Shaban, M. (2014), "Bond strength of different strengthening systems-concrete elements under freeze-thaw cycles and salt water immersion exposure", *Constr. Build. Mater.*, **70**, 399-409.

Andrawes, B. and Pozolo, A. (2011), "Transfer and development lengths in prestressed self-consolidating concrete bridge box and I-girders", Ph.D. Dissertation, University of Illinois at Urbana-Champaign, U.S.A.

ARTBA (2016), http://www.artba.org/economics/2016-u-s-deficient-bridges/.

Ary, M.I. and Kang, T.H.K. (2012), "Shear-strengthening of reinforced & prestressed concrete beams using FRP: Part I-review of previous research", *J. Concrete Struct. Mater.*, **6**(1), 41-47.

ASTM C666 (2015), *Standard Test Method for Resistance of Concrete to Rapid Freezing and Thawing*, West Conshohocken, U.S.A.

ASTM C672 (2012), *Standard Test Method for Scaling Resistance of Concrete Surfaces Exposed to Deicing Chemicals*, West Conshohocken, U.S.A.

Belarbi, A., Bae, S., Ayoub, A., Kuchma, D., Mirmiran, A. and Okeil, A. (2011), "Design of FRP systems for strengthening of concrete girders in shear", Research Report, No. 678.

Colombi, P., Fava, G. and Poggi, C. (2009), "Bond strength of CFRP-concrete elements under freeze-thaw cycles", *Compos. Struct.*, **92**(4), 973-983.

Dassault Systèmes (2013), *Abaqus 6.13 Documentation Collection*, Dassault Systèmes Simulia Corp., Rhode Island, U.S.A.

Davalos, J.F., Kodkani, S.S., Ray, I. and Lin, C. (2008), "Fracture evaluation of GFRP-concrete interfaces for freeze-thaw and wet-dry cycling", *J. Compos. Mater.*, **42**(14), 1439-1466.

Lu, X.Z., Teng, J.G., Ye, L.P. and Jiang, J.J. (2005), "Bond-slip models for FRP sheets/plates bonded to concrete", *Eng. Struct.*, **27**(6), 920-937.

MacGregor, J. and Wight, J. (2005), *Reinforced Concrete: Mechanics and Design*, 4th Edition, Prentice Hall, New Jersey, U.S.A.

Ouezdou, M.B., Bae, S. and Belarbi, A. (2008), "Effective bond length of externally bonded FRP sheets", *Proceedings of the 4th International Conference on FRP Composites in Civil Engineering*, Zurich, Switzerland, July.

Qapo, M., Dirar, S., Yang, J. and Elshafie, M.Z.E.B. (2014), "Nonlinear finite element modelling and parametric study of CFRP shear-strengthened prestressed concrete girders", *Constr. Build. Mater.*, **76**, 245-255.

QuakeWrap (2016a), P*roduct Data Sheet: QuakeBond J300SR Saturating Resin*, QuakeWrap Inc., Tucson, U.S.A.

QuakeWrap (2016b), *Product Data Sheet: QuakeWrap TU27C Carbon Fabric for Structural Strengthening*, QuakeWrap Inc., Tucson, U.S.A.

Sato, Y. and Vecchio, F.J. (2003), "Tension stiffening and crack formation in reinforced concrete members with fiber-reinforced polymer sheets", *J. Struct. Eng.*, **129**(6), 717-724.

Silva, M.A.G., Cidade, M.T., Biscaia, H. and Marreiros, R. (2014), "Composites and FRP-strengthened beams subjected to dry/wet and salt fog cycles", *J. Mater. Civil Eng.*, **26**(12), 1-12.

Subramaniam, K.V., Ali-Ahmad, M. and Ghosn, M. (2008), "Freeze-thaw degradation of FRP-concrete interface: Impact on cohesive fracture response", *Eng. Fract. Mech.*, **75**(13), 3924-3940.

Todeschini, C.E., Bianchini, A.C. and Kesler, C.E. (1964), "Behavior of concrete columns reinforced with

high strength steels", *J. Am. Concrete Inst*., **61**(6), 701-716.

You, Y., Ayoub, A. and Belarbi, A. (2011), "Three-dimensional nonlinear finite-element analysis of prestressed concrete beams strengthened with FRP composites", *J. Compos. Constr*., **15**(6), 896-907.

Younes, R., Hallal, A., Fardoun, F. and Chehade, F.H. (2012), *Comparative Review Study on Elastic Properties Modeling for Unidirectional Composite Materials*, InTech, Rijeka, Croatia.

*TK*